BER the international journal of bridge engineering management and research

Influence of Nose Position of Edge Fairing on Aerodynamic Characteristics of Box-Girder Bridge Deck

Md. Naimul Haque[1,*]; Hiroshi Katsuchi[2]; and Md. Basir Zisan[3]

Submitted: 10 June 2025 **Accepted:** 24 August 2025 **Publication date:** 10 October 2025

DOI: 10.70465/ber.v2i4.43

Abstract: Edge fairing is often applied to box-girder bridge decks to improve their aerodynamic performance, particularly in long-span bridges. A thorough understanding of the aerodynamic response and flow behavior of bridge decks with edge fairings is essential for optimal design and ensuring wind-induced safety. This study presents a numerical investigation into the influence of the nose position of edge fairings on the aerodynamic behavior of box-girder bridge decks. Two-dimensional unsteady Reynolds-averaged Navier–Stokes (URANS) simulations were performed using the *k-ω-SST* turbulence model, supported by appropriate validation studies. Both static and dynamic simulations were conducted for two configurations: edge fairings with nose-up and nose-down positions. The static analysis showed that the nose-down configuration offered superior aerodynamic performance compared to the nose-up configuration. In the nose-down position, the deck experienced reduced static wind forces with smaller fluctuations. The dynamic simulations further revealed that the nose-down fairing configuration has improved aerodynamic damping in both torsional and heaving modes. In particular, leading-edge flow reattachment was identified as the primary contributor to enhanced aerodynamic damping in the nose-down configuration. Further, the relatively larger bottom plate slope had better aeroelastic responses in the nose-down position of the edge fairing.

Author keywords: aerodynamic response; box girder; fairing; nose location; CFD; unsteady RANS; flutter derivatives; damping

Introduction

Long-span cable-supported bridges are often favored by engineers to provide wide navigation clearances. However, as the span length increases, the bridge deck becomes more flexible, raising concerns about its aeroelastic performance. To improve the aerodynamic behavior of long-span bridges, various aerodynamic countermeasures are applied to the deck. Among these, edge fairings are one of the most common and effective methods. They are used to reduce along-wind loads and suppress after-body vortex shedding, as seen in bridges such as the Deer Isle (USA), Bronx–Whitestone (USA), Hakucho (Japan), and Tempozan (Japan).

In the case of edge fairings, several shaping parameters significantly influence aerodynamic performance, including the top plate slope (θ_T), bottom plate slope (θ_B), and nose location (h/D), as illustrated in Fig. 1. Previous studies[1–3] have shown that the aerodynamic response is highly sensitive to the shape of the fairing. These studies primarily focused on experimental investigations of θ_T and θ_B, using a limited number of shape combinations due to the high cost of testing. While these efforts demonstrated the effectiveness of edge fairings in enhancing aerodynamic performance, they did not provide definitive recommendations for fairing shape design.

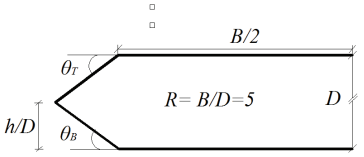

Figure 1. Geometric configuration and important shaping parameters of the considered bridge deck

Later, Haque et al.[4] conducted a comprehensive numerical study exploring a wider range of θ_T and θ_B values. They found that, for a specific range of bottom plate slopes (θ_B), the bridge deck exhibited reduced aerodynamic responses. Their study also suggested that the nose location (h/D) influences aerodynamic behavior, but its effects were not fully clarified. Interestingly, a fairing with a given combination of θ_T and θ_B can be installed either in the lower or upper half

*Corresponding Author: Md. Naimul Haque.
Email: naimul@ewubd.edu
[1]Department of Civil Engineering, East West University, Aftabnagar, Dhaka-1212, Bangladesh
[2]Department of Civil Engineering, Yokohama National University, Yokohama 240-8501, Japan
[3]Department of Civil Engineering, Chittagong University of Engineering and Technology, Raojan, Chittagong-4349, Bangladesh

Discussion period open till six months from the publication date. Please submit separate discussion for each individual paper. This paper is a part of the Vol. 2 of the International Journal of Bridge Engineering, Management and Research (BER), ISSN 3065-0569.

of the deck, referred to hereafter as the "nose-down" and "nose-up" configurations, respectively, as shown in Fig. 2. Therefore, in addition to θ_T and θ_B, the nose location (h/D) should be investigated in detail, as it may lead to practical recommendations for shaping edge fairings and optimizing bridge deck geometry. Thereafter, another study by Haque et al.[5] showed that the mean static force coefficients of bridge decks are sensitive to the nose location of the edge fairing. However, many aspects remain unexplored. In particular, the impact of nose location on the flow field and dynamic responses of the deck needs further investigation to support the design process of bridge geometries.

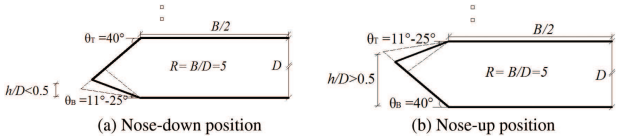

Figure 2. Considered shapes of the edge fairing and the influence of nose position (h/D) on the geometric configuration of the bridge deck

Recently, computational fluid dynamics (CFD) has become a popular and effective tool in various fields of engineering, including bridge and bluff body aerodynamics, due to its balance of accuracy and computational efficiency. The unsteady Reynolds-averaged Navier–Stokes (URANS) approach offers moderate accuracy with high efficiency. Several researchers have validated its performance and reliability,[6–16] with successful applications in the field of bridge aerodynamics.[4,6–8,16–18]

Against this background, the present study investigates the influence of the nose location (h/D) of edge fairings on the aerodynamic performance of a closed box-girder bridge deck using CFD. Two-dimensional URANS simulations employing the *k-ω-SST* turbulence model were conducted to analyze both steady-state and dynamic aerodynamic responses, as well as the associated flow fields. A comparative analysis was performed for fairings in the nose-up ($h/D > 0.5$) and nose-down ($h/D < 0.5$) configurations. For both configurations, the top (θ_T) and bottom (θ_B) plate slopes were varied from 11° to 25°, as shown in Fig. 2. Initially, force coefficients and flow field characteristics, such as pressure and velocity distributions, were examined in detail to understand the underlying aerodynamic behavior. Subsequently, for a selected fairing shape, flutter derivatives were computed to assess the influence of nose location (h/D) on the dynamic characteristics of the bridge deck. All simulations were conducted at a Reynolds number (Re) of 1.2×10^4.

Numerical Procedure

The URANS equations were used to model the flow around the bridge deck. Flow was assumed to be two-dimensional and incompressible in nature. The governing equations are as follows:

$$\frac{\partial \overline{U}_i}{\partial x_i} = 0 \tag{1}$$

$$\frac{\partial \overline{U}_i}{\partial t} + \overline{U}_j \frac{\partial \overline{U}_i}{\partial x_j} = -\frac{1}{\rho}\frac{\partial \overline{P}}{\partial x_i} + \frac{\partial}{\partial x_j}\left[\nu\left(\frac{\partial \overline{U}_i}{\partial x_j} + \frac{\partial \overline{U}_j}{\partial x_i}\right) - \left(\overline{u_i' u_j'}\right)\right] \tag{2}$$

where $\overline{U}_i$ and x_i are the averaged velocity and position vectors, respectively, t is the time, $\overline{P}$ is the averaged pressure, ρ is the air density, and ν is the fluid viscosity. Due to the time-averaging process, a new variable $\overline{u_i' u_j'}$ appeared, known as Reynolds stress, which needs modeling to close the equation, a process known as turbulence modeling. Turbulence modeling was attained by *k-ω-SST*, a two-equation turbulence model.[19]

A forced vibration dynamic simulation was also conducted to extract the flutter derivatives. In these simulations, the motion of the bridge deck boundaries was modeled by adapting the computational grid, implemented through the arbitrary Lagrangian–Eulerian formulation of the URANS equations.[20,21] This approach allowed the mesh to move with the oscillating structure, capturing the fluid–structure interaction more accurately. As a result, the governing equations were modified accordingly

$$\frac{\partial \left(\overline{U}_i - \overline{U}_{gi}\right)}{\partial x_i} = 0 \tag{3}$$

$$\frac{\partial \overline{U}_i}{\partial t} + \overline{U}_j \frac{\partial \left(\overline{U}_i - \overline{U}_{gi}\right)}{\partial x_j} = -\frac{1}{\rho}\frac{\partial \overline{P}}{\partial x_i} + \frac{\partial}{\partial x_j}\left[\nu\left(\frac{\partial \overline{U}_i}{\partial x_j} + \frac{\partial \overline{U}_j}{\partial x_i}\right) - \left(\overline{u_i' u_j'}\right)\right] \tag{4}$$

where $\overline{U}_{gi}$ is the grid velocity in the ith direction.

All the governing equations described above were discretized using the finite volume method, and the open-source CFD software OpenFOAM was used as the solver. The convective and diffusive terms in the governing equations were discretized using second-order accurate central differencing schemes. For time integration, the second-order accurate backward differentiation formula method was employed. The PISO (Pressure Implicit with Splitting of Operator) algorithm was used to solve the discretized equations. During the dynamic simulations, the pressure–velocity coupling was achieved using the PIMPLE (Pressure Implicit with Momentum Prediction and Localized Enrichment) algorithm, a hybrid of the PISO and SIMPLE (Semi-Implicit Method for Pressure-Linked Equations) methods, offering improved stability and convergence for transient simulations. To ensure numerical stability, the maximum Courant number (C_o) was maintained well below 1 throughout the simulations.

The computational domain size and mesh layout are illustrated in Fig. 3. The domain size was chosen based on recommendations from previous studies and validated in[16,22]. It was made sufficiently large to minimize boundary interference with the flow field. A no-slip boundary condition ($\partial u/\partial y \neq 0$, $v = 0$) was applied on the bridge deck surface. At the domain inlet, a Dirichlet boundary condition

was applied for velocity ($u = U$, $v = 0$), and a Neumann condition ($\partial p/\partial n = 0$) was used for pressure. At the outlet, Neumann conditions were applied for velocity, and Dirichlet conditions for pressure. Slip boundary conditions ($\partial u/\partial y = 0$, $v = 0$) were applied at the top and bottom boundaries of the domain.

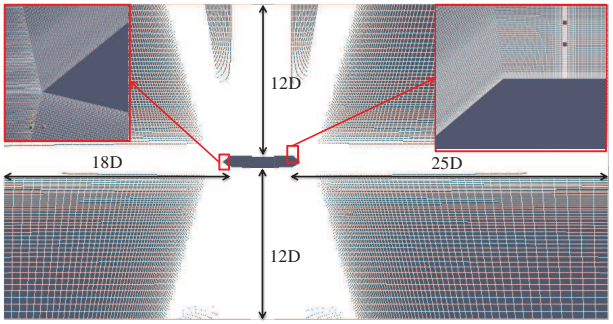

Figure 3. Meshing details of the bridge deck section. All the dimensions are normalized with the height of the bridge deck (D)

A body-fitted structured grid system was used for spatial discretization, as shown in Fig. 3. The first grid height (y) normal to the deck surface was selected such that the wall-adjacent cells remained within the viscous sub-layer ($y^+ \leq 5$). Grid spacing was gradually increased away from the surface using a constant growth factor of 1.05 in all directions. Overall, the bridge deck maintained an average y^+ value well below 5. Only in a small region near the leading edge corner of the top surface did the maximum y^+ slightly exceed 5. Since the primary objective of this study was to compare the relative aerodynamic responses of various deck shapes, maintaining a consistent grid resolution, particularly in terms of y^+ values, was essential for a valid comparison. Accordingly, all simulations ensured that the variation in y^+ values remained within approximately 5%, regardless of fairing shape variations.

Aerodynamic Analysis

In the static analysis, the main parameter of interest was the steady-state force coefficients. The steady-state force coefficients such as drag (C_D), lift (C_L), moment (C_M), and Strouhal number (S_t) were defined as follows:

$$C_D = \frac{F_D}{1/2\rho U^2 D} \text{ (downstream positive)} \tag{5}$$

$$C_L = \frac{F_L}{1/2\rho U^2 B} \text{ (upward positive)} \tag{6}$$

$$C_M = \frac{F_M}{1/2\rho U^2 B^2} \text{ (anticlockwise positive)} \tag{7}$$

$$S_t = \frac{fB}{U} \tag{8}$$

where F_D, F_L, and F_M are the drag, lift, and moment forces acting per unit length on the bridge deck, respectively, and f is the shedding frequency. Both the mean and root mean square (rms) values of the time-varying force coefficients were evaluated. In all cases, the rms values were calculated from the zero-mean force coefficient time histories.

The main goal of dynamic simulation is to extract the flutter derivatives to judge the aerodynamic characteristics of the bridge deck. The aerodynamic lift and moment forces are expressed by the following expression, as mentioned in Simiu and Scanlan:[23]

$$L(t) = \frac{1}{2}\cdot\rho\cdot U^2\cdot B_1\cdot\left[k\cdot H_1^*\cdot\frac{\dot{\eta}}{U} + k\cdot H_2^*\cdot B_1\cdot\frac{\dot{\alpha}}{U} + k^2\cdot H_3^*\cdot\alpha + k^2\cdot H_4^*\cdot\frac{\eta}{B_1}\right] \tag{9}$$

$$M(t) = \frac{1}{2}\cdot\rho\cdot U^2\cdot B_1^2\cdot\left[k\cdot A_1^*\cdot\frac{\dot{\eta}}{U} + k\cdot A_2^*\cdot B_1\cdot\frac{\dot{\alpha}}{U} + k^2\cdot A_3^*\cdot\alpha + k^2\cdot A_4^*\cdot\frac{\eta}{B_1}\right] \tag{10}$$

where $L(t)$ and $M(t)$ are the time-varying self-excited lift force and moment per unit span of the bridge deck, respectively; ρ is the air density; U is the mean wind speed; k is the reduced frequency, ($k = B_1.\omega/U$); ω is the circular frequency, ($2.\pi.f$); B_1 is the full width of the bridge deck; η is the heaving displacement; α is the torsional displacement; the dot ($\dot{}$) represents first time derivatives; and H_i^* and A_i^* are the aerodynamic coefficients known as flutter derivatives in heaving and torsional motions, respectively. The methodology to extract the flutter derivatives through forced vibration simulation was discussed in detail in previous numerical works;[9,12–15,24,25] hence, the discussion is not deepened here. The work done by the unsteady pressure provides an in-depth understanding of the complex fluid–structure interaction under torsional mode and was calculated by the following equation:

$$C_{PI}\cdot r = \left(\frac{x}{B_1}\right)\cdot|C_P(x)|\cdot Sin\,\varphi(x) \tag{11}$$

Here, r represents the normalized distance from the center of the bridge deck toward either side. The function $\varphi(x)$ denotes the phase difference between the maximum relative angle of attack of the bridge deck and the maximum negative pressure at a distance x from the deck center. $C_p(x)$ is the magnitude of the unsteady pressure, and C_{pi} is the imaginary component of the unsteady pressure. A positive value of the product $C_{pi}\cdot r$ indicates an excitation force acting at the leading edge of the top surface of the bridge deck, while a negative value indicates damping. At the trailing edge of the top surface, the sign convention is reversed. For the bottom surface of the deck, the sign convention is also reversed relative to the top surface, both at the leading and trailing edges.

The model was excited with a one degree of freedom torsional (α) motion of periodic vibration to extract the flutter derivatives. A torsional (α_o) amplitude of 1° was utilized. The reduced velocity (U/fB_1) was altered by changing the frequency of vibration (f_α) only. The heaving motion flutter derivatives were calculated from the interdependency

relationships among the flutter derivatives proposed by Matsumoto[26] to reduce time and computational cost. Previously, Tubin[27] also checked this type of interdependency relationship among the flutter derivatives experimentally and found very good compatibility for a streamlined bridge deck. Later, Nieto et al.[9] checked those relationships given by Tubin[27] numerically and recommended for further applicability to reduce the computational load due to their high efficiency.

Validation

The performance of the utilized numerical model and setup for simulating steady-state responses had already been checked previously.[4,16,18,22,25,28] However, in the present study, along with the steady-state response, the dynamic response, such as the flutter derivatives, was also taken into consideration. Therefore, the performance of the present numerical method should be checked for simulating dynamic responses such as the flutter derivatives around a bluff section.

We conducted the simulation for the rectangular cylinder with a side ratio (R) of 5. Normally, the rectangular cylinder experiences quite a large flow separation as compared to the bridge deck with fairing. Therefore, if the present numerical setup can reproduce the dynamic responses accurately for the rectangular cylinder of a side ratio (R) of 5, that would be sufficient for the considered bridge deck with fairing. Simulations were carried out at a Reynolds number (R_{eB}) of 5.0×10^4 with a torsional amplitude (α_o) of 1°.

The extracted flutter derivatives are presented in Fig. 4 and compared with the experimental results reported by Matsumoto.[26] A reasonable agreement can be observed between the present numerical results and the past experimental data. However, noticeable discrepancies are found in the flutter derivatives H_2^* and A_2^* when compared to other derivatives. Similar discrepancies have also been reported in previous studies,[7,9,13,29] suggesting this may be a common challenge in numerical–experimental comparisons. Despite these differences, the overall trends and general behavior of the flutter derivatives were accurately reproduced. Furthermore, the flutter derivatives for the heaving mode calculated using interdependency relationships also show good agreement with the experimental data, similar to the torsional mode derivatives.

In particular, as seen in Fig. 4, the present results show closer agreement with the flutter derivatives reported by Sarker et al.,[30] while some differences are observed between the results of Matsumoto[26] and Sarker et al.[30] themselves. Nonetheless, since the primary objective of this study is to perform a relative comparison of flutter derivatives across different bridge deck configurations, the level of accuracy achieved is sufficient to evaluate the influence of the nose location (h/D) on aerodynamic responses.

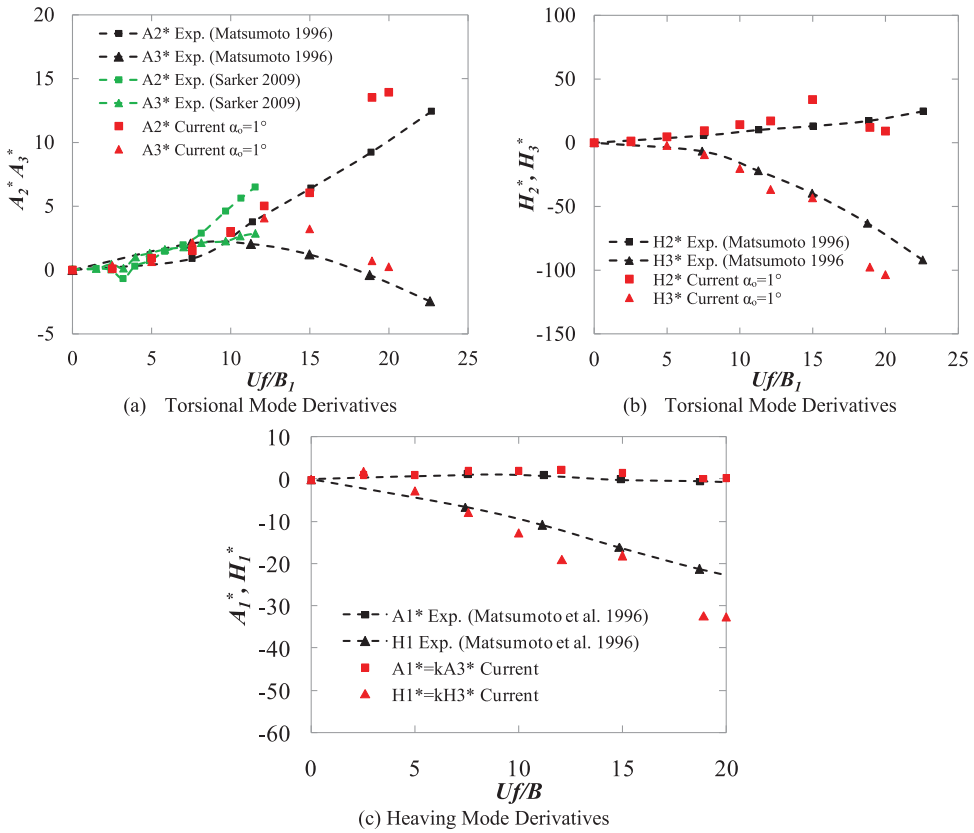

Figure 4. Important flutter derivatives of the rectangular cylinder having side ratio (R) of 5: (a, b) Calculated from the forced torsional oscillation and compared with the experimental results of Matsumoto[26] and Sarkar et al.[30] and (c) calculated from the interdependency relationships[26]

Steady-State Response

Steady-state force coefficient

Simulations were conducted for the bridge deck configurations shown in Fig. 2. In the nose-down configuration, the top plate slope (θ_T) was fixed at 40°, while the bottom plate slope (θ_B) was varied from 11° to 25°. Conversely, in the nose-up configuration, the bottom plate slope (θ_B) was fixed at 40°, and the top plate slope (θ_T) was varied within the same range (11°–25°).

Fig. 5 compares the mean values of static aerodynamic coefficients for these two configurations. The results clearly indicate that the nose location (h/D) has a significant influence on the steady-state force coefficients. For any given value of θ_T or θ_B, the fairing in the nose-down position consistently shows lower aerodynamic responses than that in the nose-up position. Both the mean drag coefficient (C_D) and the mean lift coefficient (C_L) demonstrate improved performance in the nose-down configuration, characterized by reduced drag and more favorable lift behavior. For the nose-down position, the bridge deck experiences a counterclockwise aerodynamic moment, whereas in the nose-up position, it experiences a clockwise moment. The magnitude of this moment increases as the plate slope decreases in both configurations. While the sign of the moment coefficient (C_M) has limited aerodynamic significance, the sign of the lift coefficient (C_L) is particularly important in bridge aerodynamics. A negative lift force (downward acting) is beneficial, as it increases cable tension and enhances the aerodynamic stability of the bridge deck. This effect is more pronounced in the nose-down configuration, indicating superior aerodynamic performance.

The rms values of the aerodynamic coefficients, which reflect the deck's dynamic response to wind excitation, are compared in Fig. 6. Similar to the mean values, the rms coefficients are generally lower for the nose-down configuration. As shown in Figs. 6a and 6b, for any value of θ_T or θ_B, the nose-down configuration exhibits slightly smaller fluctuations caused by after-body vortex shedding. The Strouhal number (S_t), which represents the vortex shedding frequency, exhibits comparatively lower sensitivity to changes in the nose location. However, for smaller plate slopes (θ_T or θ_B), the nose-down configuration shows higher Strouhal numbers, indicating a more streamlined behavior and a higher vortex shedding frequency.

This section has quantitatively discussed the influence of nose location (h/D) on the steady-state aerodynamic force coefficients. In the following section, a detailed analysis of the steady-state flow field is presented for a specific fairing shape, since the observed influence of nose location on force coefficients remains consistent across different values of θ_T and θ_B.

Flow behavior of bridge deck

The flow field was analyzed for two shapes of fairings viz.: i) Nose-up position (θ_T12–θ_B40; $h/D > 0.5$) and ii) nose-down position (θ_T40–θ_B12; $h/D < 0.5$). The mean surface pressures for these cases are shown in Fig. 7. The nose

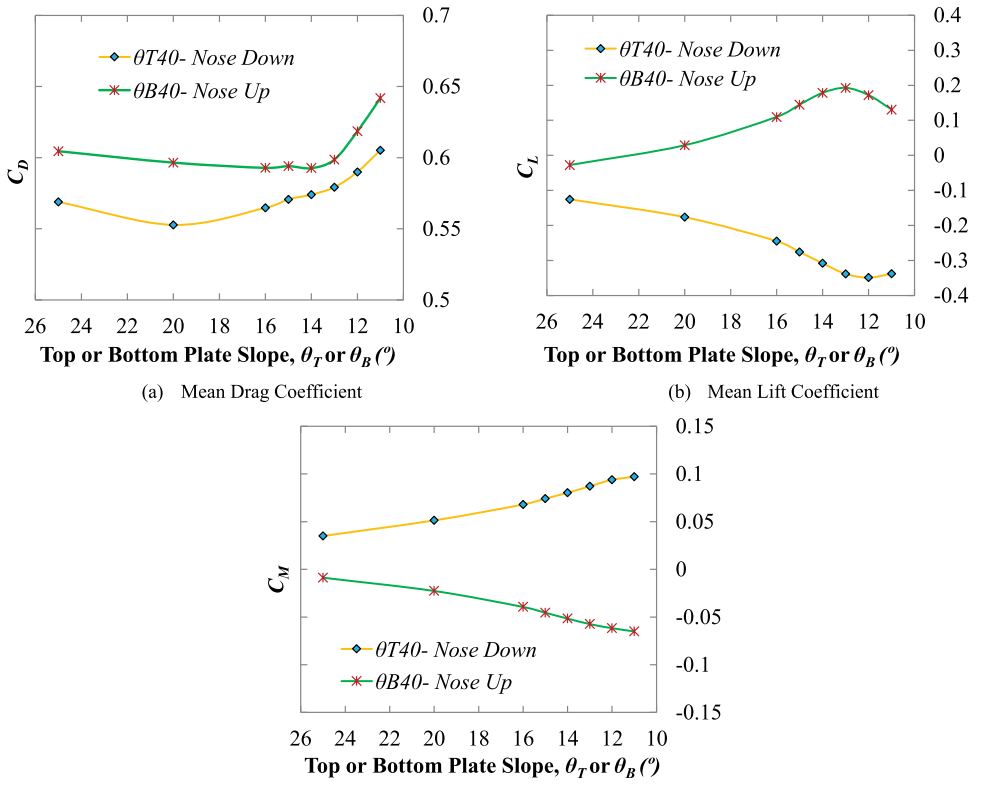

Figure 5. Mean force coefficients for variation fairing's angle with nose-down and nose-up positions

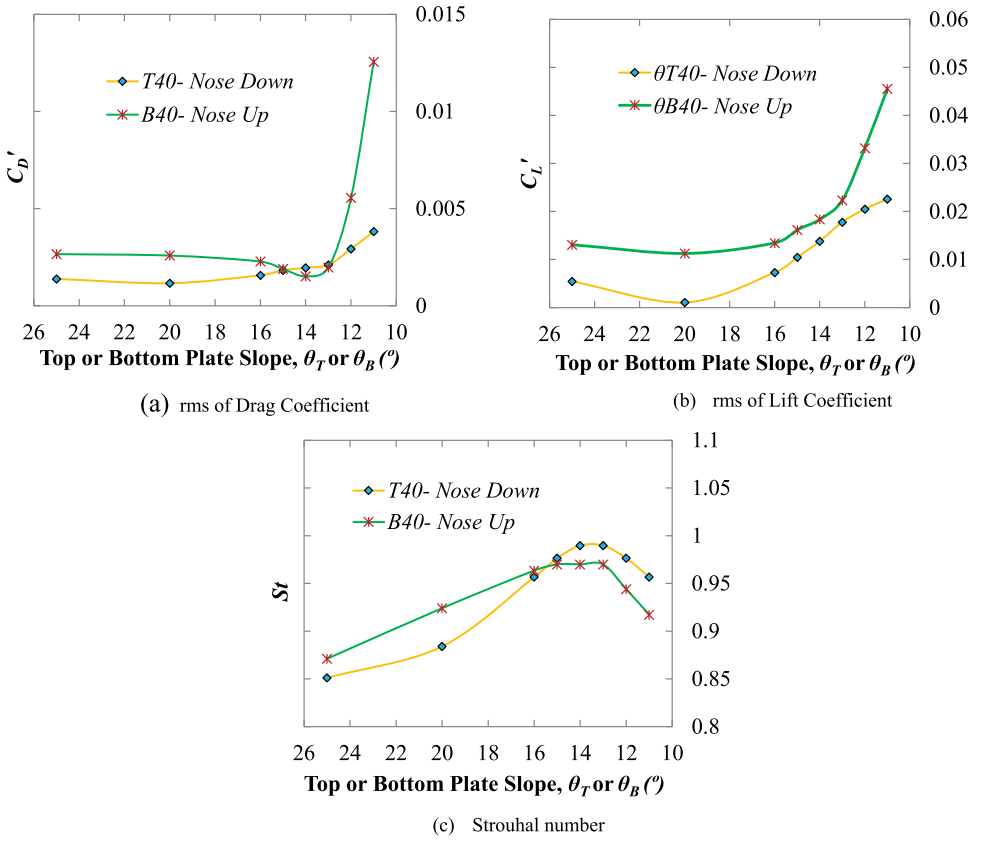

Figure 6. rms of force coefficients and Strouhal number for variation fairing's angle with nose-down and nose-up positions

location (h/D) primarily influences the pressure distribution near the leading edge of the deck, while the trailing edge is less affected. In the nose-down configuration ($h/D < 0.5$), a strong negative pressure appears on the leading-edge bottom surface, accompanied by positive pressure on the leading-edge top surface, resulting in a positive moment coefficient (counterclockwise moment). Conversely, in the nose-up configuration ($h/D > 0.5$), the moment coefficient is negative (clockwise moment) due to reversed pressure patterns.

When the fairing is in the nose-down position, the entire bottom surface of the deck experiences negative pressure (suction), which generates a negative lift force coefficient. Shifting the nose to the upper side reverses this effect, producing a positive lift due to suction on the top surface. The rms surface pressures, compared in Fig. 8, exhibit a contrasting behavior. The rms values are mainly influenced near the trailing edge, where the nose-up configuration ($h/D > 0.5$) shows slightly higher-pressure fluctuations than the nose-down case ($h/D < 0.5$). Instantaneous velocity fields over one lift cycle for the nose-down and nose-up configurations are illustrated in Figs. 9 and 10, respectively. These figures clearly show the leading-edge shear layer separation and reattachment, along with after-body vortex shedding. For the nose-down position ($h/D < 0.5$), significant suction occurs due to flow separation on the bottom surface near the leading edge. This bottom surface separation is more pronounced than the leading-edge top surface separation in the same configuration. Between the two positions, the

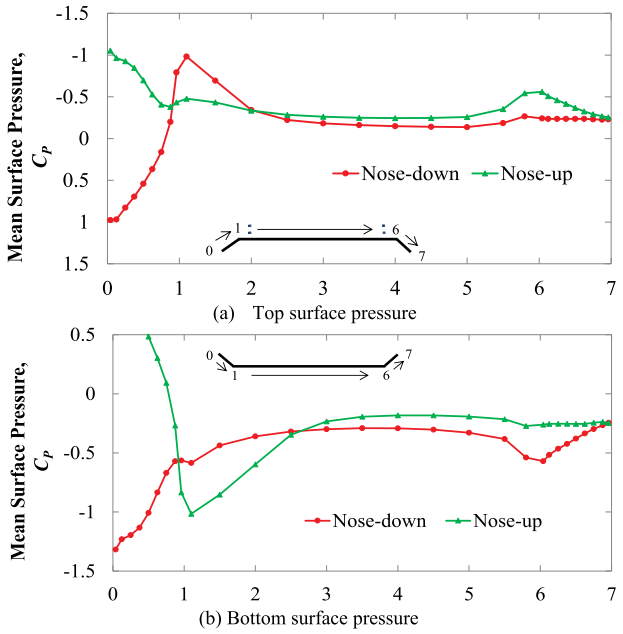

Figure 7. Mean surface pressure distribution around the bridge deck

nose-up configuration ($h/D > 0.5$) exhibits more prominent leading-edge flow separation compared to the nose-down case. Notably, the nose location also influences the size of the after-body vortex. It is observed that the vortex on the

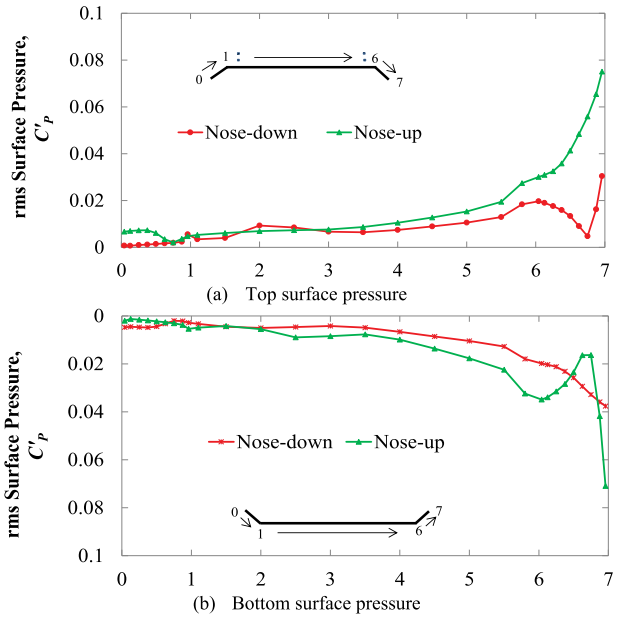

Figure 8. rms surface pressure distribution around the bridge deck

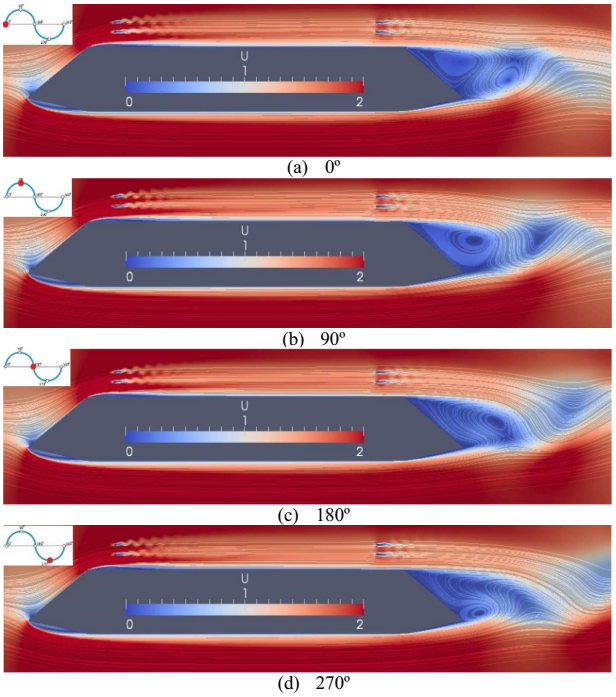

Figure 9. Velocity field around the bridge deck for nose-down condition along one lift cycle

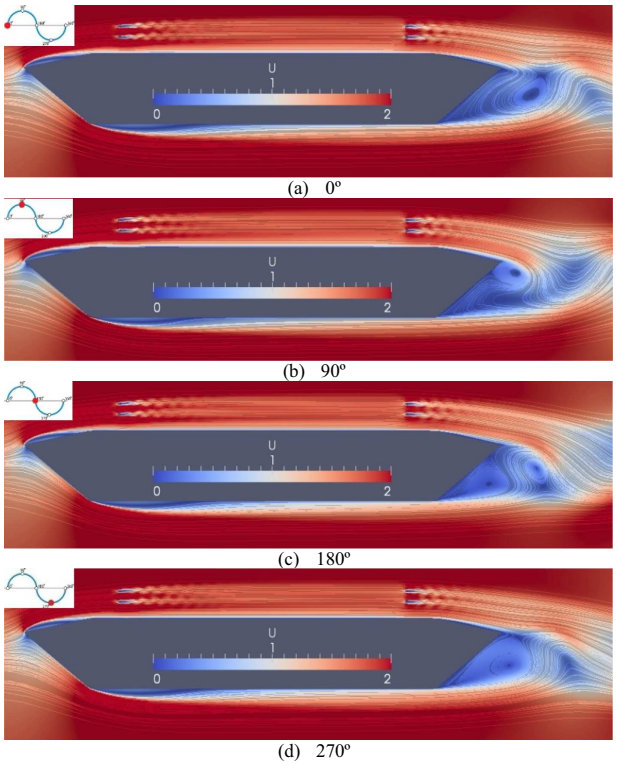

Figure 10. Velocity field around the bridge deck for nose-up condition along one lift cycle

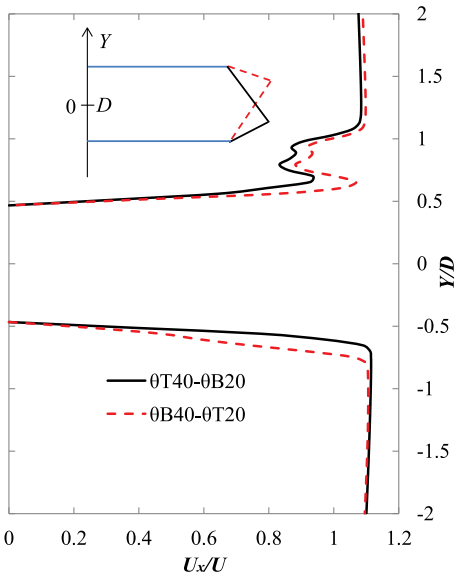

Figure 11. Velocity field around the bridge deck for nose-up condition along one lift cycle

side where the nose is located is smaller than the vortex on the opposite side.

Fig. 11 shows the velocity distributions along the vertical line at the mid-deck section. In both configurations, the velocity distribution along the bottom surface is relatively smooth, while the top surface distribution is more irregular due to the presence of the handrail. As the nose moves downward, the flow velocity along the bottom deck surface increases, enhancing suction and thereby increasing the deck's negative lift. For the nose-down position ($h/D < 0.5$), the shear layer on the bottom surface of the deck is thinner than that on the top surface. These shear layers separate at the trailing edge and roll up to form vortex shedding. The bridge deck with a nose-up position exhibits similar shear layer behavior but in the opposite sense.

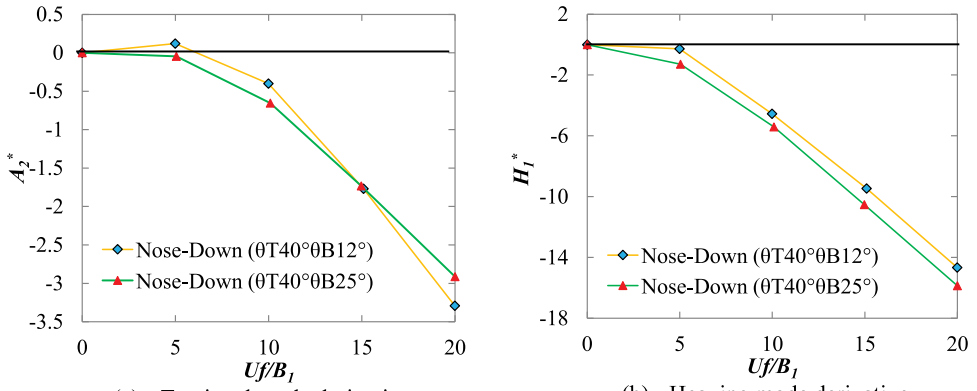

(a) Torsional mode derivative (b) Heaving mode derivative

Figure 12. Flutter derivatives for nose-down positions for two configurations (θ_T40–θ_B12 *and* θ_T40–θ_B25): a) torsional mode derivative (computed directly), and b) heaving mode derivative (computed based on interdependency relationship)

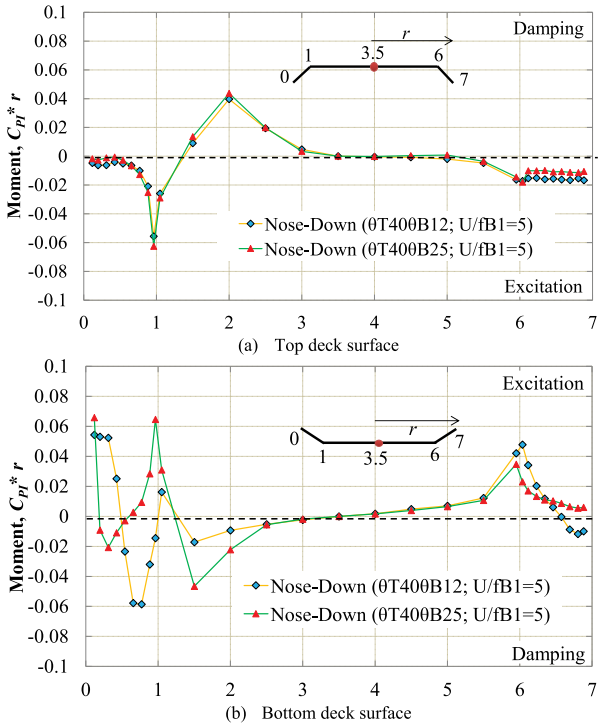

Figure 13. Influence of bottom plate slope (θ_B) for nose-down position on work done by unsteady pressure in torsional mode at low reduced velocity ($U/fB_1 = 5$)

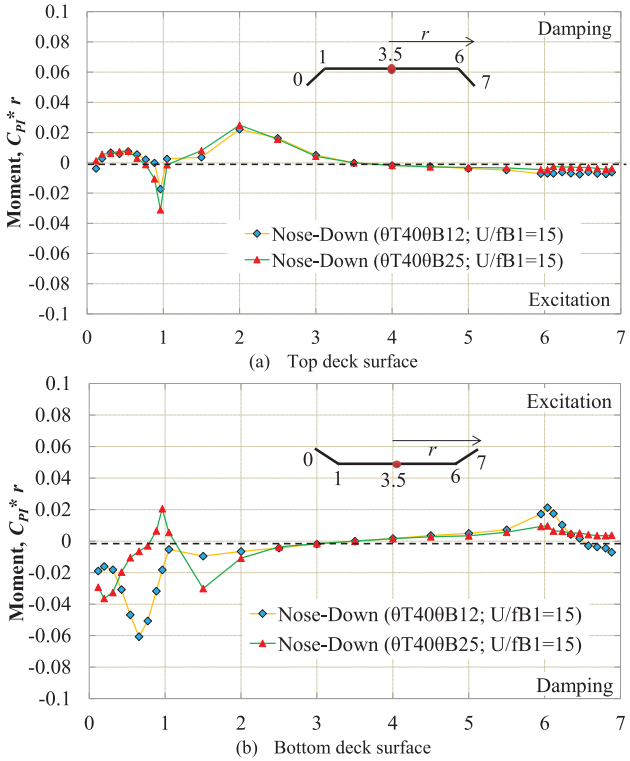

Figure 14. Influence of bottom plate slope for nose-down position on work done by unsteady pressure in torsional mode ($U/fB_1 = 15$)

Dynamic Responses

In the previous section, the static aerodynamic responses of the bridge deck with both nose-up and nose-down configurations were analyzed, revealing that the nose-down position offers improved static aerodynamic performance. Based on this finding, dynamic simulations were conducted for the nose-down configuration only, due to the high computational cost of such simulations. Two orientations of nose-down positions were selected with different bottom plate slopes (θ_B). Dynamic simulations were carried out for the nose-down configurations of $\theta_T40°$–$\theta_B12°$ and $\theta_T40°$–$\theta_B25°$ to evaluate flutter derivatives and the work done by unsteady pressure. The $\theta_T40°$–$\theta_B25°$ orientation has a relatively higher nose position as compared to the $\theta_T40°$–$\theta_B12°$ orientation. To simplify the analysis, handrails were excluded, and the forced vibration simulation was carried out on the basic deck section only.

Fig. 12 presents the key flutter derivatives A_2^* and H_1^* for the nose-down configurations ($\theta_T40°$–$\theta_B12°$ and $\theta_T40°$–$\theta_B25°$). The derivative A_2^* was calculated directly through numerical simulation, while H_1^* was obtained using

interdependency relationships. These two derivatives are particularly important, as they provide critical insights into the torsional and heaving mode vibrations of bridge decks. The results demonstrate that both of the nose-down configurations exhibit improved flutter performance. At a low reduced velocity ($U/fB_1 = 5$), the nose-down configuration with a smaller bottom plate slope ($\theta_T = 40°$, $\theta_B = 12°$) exhibited a positive value of A_2^*, indicating torsional instability. In contrast, the bridge deck with a steeper bottom plate slope ($\theta_T = 40°$, $\theta_B = 25°$) in the nose-down position remained aerodynamically stable across the entire range of considered reduced velocities. At higher reduced velocities, both torsional and heaving mode stabilities improve, confirming the favorable dynamic response of the bridge deck.

The work done by unsteady pressure in the torsional mode, as discussed in Section 3, is presented in Figs. 13 and 14 for both low ($U/fB_1 = 5$) and high ($U/fB_1 = 15$) reduced velocities. These figures show that leading-edge flow separation on both the top and bottom surfaces of the deck contributes to aerodynamic excitation, while flow reattachment acts as a source of aerodynamic damping. Additionally, trailing-edge flow separation near the fairing on both surfaces serves as another source of excitation.

At the lower reduced velocity ($U/fB_1 = 5$), variations in the bottom plate slope (θ_B) primarily affect the bottom surface near the leading edge. Increasing θ_B while maintaining the nose-down configuration enhances the damping magnitude at the bottom surface reattachment region. This results in improved torsional stability due to stronger aerodynamic damping. At higher reduced velocity ($U/fB_1 = 15$), the overall excitation and damping patterns remain similar, although the magnitudes are generally reduced. The most noticeable changes occur near the leading edge on the bottom surface, where almost all the area becomes aerodynamic damping and enhances the torsional stability further. In the nose-down position, θ_B has minimal impact on the top surface flow but significantly influences the bottom surface. As θ_B increases from 15° to 25°, the region of leading-edge damping shifts downstream (in the direction of flow) and grows in magnitude, while excitation near the trailing edge decreases. These effects collectively enhance the aerodynamic performance of the bridge deck.

Conclusions

The influence of the edge fairing's nose location (h/D) on the aerodynamic response of a box-girder bridge deck was investigated using two-dimensional unsteady RANS simulations. The fairing shapes were varied by altering the top (θ_T) and bottom (θ_B) plate slopes to assess the effect of nose location on both static and dynamic aerodynamic behaviors. The results demonstrated that the nose-down configuration provides superior aerodynamic performance. In this configuration, the bridge deck experiences reduced aerodynamic forces and smaller fluctuations, contributing to improved stability. When the fairing nose is positioned downward, flow separation at the leading-edge bottom surface is minimized. The flow reattaches downstream and then separates again at the trailing edge, forming a controlled after-body vortex shedding pattern. Additionally, the bottom surface of the deck experiences faster flow and a thinner shear layer, which generates a stronger downward lift force and further reduces aerodynamic fluctuations.

In terms of dynamic behavior, the nose-down configuration offers clear advantages, providing greater aerodynamic damping in both heaving and torsional vibration modes. This damping effect is sustained and even enhanced at higher reduced velocities, indicating improved aeroelastic stability. Analysis of the unsteady pressure distributions reveals that aerodynamic damping primarily originates in the leading-edge flow reattachment zone, while aerodynamic excitation is associated with flow separation at both the leading and trailing edges. Among the nose-down configurations, a higher bottom plate slope of 25° was found to be more advantageous compared to a slope of 12°. At this larger bottom plate slope (θ_B) of the edge fairing, the region of damping on the bottom deck surface shifts inward in the direction of the flow, with increased magnitude. Simultaneously, excitation at the trailing edge is reduced, resulting in improved aerodynamic performance.

Acknowledgements

Not applicable.

Authors' Contributions

The first author was responsible for the formulation of the problem, the analyses of numerical results, and the writing. The second author directed the whole work, and the third author helped in writing and formatting.

Funding

Not applicable.

Competing Interests

The authors declare that they have no competing interests.

References

[1] Nagao F, Utsunomiya H, Oryu T, Manabe S. Aerodynamic efficiency of triangular fairing on box girder bridge. *J Wind Eng Ind Aerodyn*. 1993;49(1-3):565–574. doi:10.1016/0167-6105(93)90050-x.

[2] De Miranda M, Bartoli G. Aerodynamic optimization of decks of cable-stayed bridges. Cable-supported bridges—challenging technical limits. In: *Proceeding of the IABSE Conference*; June 12–14, 2001; Seoul Korea, pp. 34–41.

[3] Sukamta, Nagao F, Noda M, Muneta K. Aerodynamic stabilizing mechanism of a cable stayed bridge with two edge box girder. In: *Proceedings of the 6th International Colloquium on Bluff Body Aerodynamics and Applications*; July 20–24, 2008; Milano, Italy.

[4] Haque MN, Katsuchi H, Yamada H, Nishio M. Investigation of edge fairing shaping effects on aerodynamic response of long-span bridge deck by unsteady RANS. *Arch Civil Mech Eng*. 2016;16(04):888–900. doi:10.1016/j.acme.2016.06.007.

[5] Haque MN, Katsuchi H, ZisanNagao MB. Geometric effects of edge fairing on aerodynamic characteristics of box girder bridge deck: influence of nose position. In: *Proceedings of International Conference on Structural Engineering Research (iCSER-2019)*; January 19–23, 2019; Dhaka, Bangladesh.

[6] Bruno L, Mancini G. Importance of deck details in bridge aerodynamics. *Struct Eng Int*. 2002;12(4):289–294. doi:10.2749/101686602777965234.

[7] Sarwar MW, Ishihara T, Shimada K, Yamasaki Y, Ikeda T. Prediction of aerodynamic characteristics of a box girder bridge section using the LES turbulence model. *J Wind Eng Ind Aerodyn*. 2008;96(10-11):1895–1911. doi:10.1016/j.jweia.2008.02.015.

[8] Sarwar MW, Ishihara T. Numerical study on suppression of vortex-induced vibrations of a box girder bridge section by aerodynamic countermeasures. *J Wind Eng Ind Aerodyn*. 2010;98(12):701–711. doi:10.1016/j.jweia.2010.06.001.

[9] Nieto F, Owen JS, Hargreaves DM, Hernandez S. Bridge deck flutter derivatives: efficient numerical evaluation exploiting their independencies. *J Wind Eng Ind Aerodyn*. 2015;136(4):138–150. doi:10.1016/j.jweia.2014.11.006.

[10] Mannini C, Šoda A, Ralph V, Schewe G. Unsteady RANS simulation of flow around a bridge section. *J Wind Eng Ind Aerodyn*. 2010;98(12):742–753. doi:10.1016/j.jweia.2010.06.010.

[11] Mannini C, Šoda A, Schewe G. Unsteady RANS modeling of flow past a rectangular cylinder: investigation of Reynolds number effects. *Comput Fluids*. 2010;39(09):1609–1624. doi:10.1016/j.compfluid.2010.05.014.

[12] Brusiani F, De Miranda S, Patruno L, Ubertini F, Vaona P. On the evaluation of bridge deck flutter derivatives using RANS turbulence model. *J Wind Eng Ind Aerodyn*. 2013;119:39–47. doi:10.1016/j.jweia.2013.05.002.

[13] Miranda SD, Patruno L, Ubertini F, Vairo G. On the identifications of the flutter derivatives of bridge deck via RANS turbulence models: benchmarking on rectangular prisms. *Eng Struct*. 2014;76:359–370. doi:10.1016/j.engstruct.2014.07.027.

[14] Patruno L. Accuracy of numerically evaluated flutter derivatives of bridge deck sections using RANS: effects on the flutter onset velocity. *Eng Struct*. 2015;89:49–65. doi:10.1016/j.engstruct.2015.01.034.

[15] Šarkić A, Fisch R, Höffer R, Bletzinger K. Bridge flutter derivatives based on computed, validated pressure fields. *J Wind Eng Ind Aerodyn*. 2012;104–106(2–3):141–151. doi:10.1016/j.jweia.2012.02.033.

[16] Haque MN, Katsuchi H, Yamada H, Nishio M. Strategy to develop efficient grid system for flow analysis around two-dimensional bluff bodies. *KSCE J Civil Eng*. 2015;20(05):1–12. doi:10.1007/s12205-015-0696-2.

[17] Shirai S, Ueda T. Aerodynamic simulation by CFD of flat box girder of super-long span suspension bridge. In: *Proceedings of Fifth Asia-Pacific Conference on Wind Engineering*; 2001; Kyoto, Japan, pp. 21–24.

[18] Haque MN, Katsuchi H, Yamada Y. Bottom plate slope effects on aerodynamic behaviour of hexagonal cross-section bridge deck. Wind engineering for natural hazards: modeling, simulation and mitigation of windstorm impact on critical infrastructure. *Trends Eng Mech Spec Publ No 3*. 2018:205–223. doi:10.1061/9780784415153.ch11.

[19] Menter FR. Two-equation eddy-viscosity turbulence models for engineering application. *AIAA J*. 1994;32(8):1589–1605. doi:10.2514/3.12149.

[20] Donea J, Huerta A, Ponthot Ph J, Rodríguez-Ferran A. Encyclopedia of computational mechanics, Volume 2 solids and structures. In: *Chapter Arbitrary Lagrangian–Eulerian Methods*. Chichester: Wiley; 2004:413–438.

[21] Ferziger JH, Perić M. *Computational Methods for Fluid Dynamics*. 2nd ed. Berlin, Heidelberg: Springer; 2002.

[22] Haque MN, Katsuchi H, Yamada Y, Nishio M. Flow field analysis of a pentagonal-shaped bridge deck by unsteady RANS. *Eng Appl Comput Fluid Mech*. 2015;10(1):1–16. doi:10.1080/19942060.2015.1099569.

[23] Simiu E, Scalan RH. *Wind Effects on Structures: Fundamentals and Applications to Design*. 3rd ed. New York: John Wiley & Sons Publisher; 1996.

[24] Larsen A, Walther JH. Discrete vortex simulation of flow around five generic bridge deck sections. *J Wind Eng Ind Aerodyn*. 1998;77–78:591–602. doi:10.1016/s0167-6105(98)00175-5.

[25] Haque MN, Katsuchi H. Influence of separation interference method on aerodynamic responses of a pentagonal shaped bridge deck. *Structures*. 2018;16(3):27–35. doi:10.1016/j.istruc.2018.08.010.

[26] Matsumoto M. Aerodynamic damping of prisms. *J Wind Eng Ind Aerodyn*. 1996;59(2-3):159–175. doi:10.1016/0167-6105(96)00005-0.

[27] Tubin F. Relationships among aerodynamic admittance functions, flutter derivatives and static coefficients for long-span bridges. *J Wind Eng Ind Aerodyn*. 2005;93(12):929–950. doi:10.1016/j.jweia.2005.09.002.

[28] Haque MN, Katsuchi H, Yamada H, Kim H. Influence of geometric configuration on aerodynamics of streamlined bridge deck by unsteady RANS. *Wind Struct*. 2019;28:331–345.

[29] Huang L, Liao H, Wang B, Li Y. Numerical simulation for aerodynamic derivatives of bridge deck. *Simul, Model, Pract Theor*. 2009;17(4):719–729. doi:10.1016/j.simpat.2008.12.004.

[30] Sarkar PP, Caracogila L, Haan FL, Sato H, Murakoshi J. Comparative and sensitivity study of flutter derivatives of selected bridge deck sections, Part 1: analysis of inter-laboratory experimental data. *Eng Struct*. 2009;31(1):158–169. doi:10.1016/j.engstruct.2008.07.020.